Journal of Solid State Chemistry 184 (2011) 3135–3143

Contents lists available at SciVerse ScienceDirect

Journal of Solid State Chemistry

journal homepage: www.elsevier.com/locate/jssc

Exfoliation and thermal transformations of Nb-substituted layered titanates

Haiyan Song [a], Anja O. Sjåstad [a], Helmer Fjellvåg [a], Hiroshi Okamoto [a], Ørnulv B. Vistad [b], Bjørnar Arstad [b], Poul Norby [a,c,*]

[a] Department of Chemistry and Centre for Materials Science and Nanotechnology, University of Oslo, P.O. Box 1033, Blindern, N-0315 Oslo, Norway
[b] SINTEF Materials and Chemistry, P.O. Box 124, Blindern, N-0314 Oslo, Norway
[c] Materials Research Division, Risø National Laboratory for Sustainable Energy, Technical University of Denmark, P.O. Box 49, DK-4000 Roskilde, Denmark

ARTICLE INFO

Article history:
Received 21 June 2011
Received in revised form
29 August 2011
Accepted 30 August 2011
Available online 12 September 2011

Keywords:
Nb-substitution
Nanosheets
Exfoliation
Restacking
Ultrasonication

ABSTRACT

Single-layer Nb-substituted titanate nanosheets of ca. 1 nm thickness were obtained by exfoliating tetrabutylammonium (TBA)-intercalated Nb-substituted titanates in water. AFM images and turbidity measurements reveal that the exfoliated nanosheets crack and corrugate when sonicated. Upon heating, the thermal transformation into anatase and further to rutile is retarded. This suppression of the phase transition upon higher valent substitution may promote technological applications of anatase thin films, hereunder development of films with TCO properties. Depending on the oxygen partial pressure during the transformation, the Nb-substitution into TiO_2 provokes different defect situations and also electronic properties. At reducing conditions, Nb is incorporated as Nb^V and an equivalent amount of Ti^{IV} is transformed to Ti^{III} as evidenced by XPS. Magnetic susceptibility data show accordingly paramagnetic behavior. For samples heated in air Ti^{IV} and Nb^V cations prevail, the latter is compensated by cation vacancies. ^{93}Nb MAS NMR data prove that Nb is finely dispersed into the transformed (Ti,Nb)O_2 oxide matrices without sign of Nb_2O_5 (nano)precipitates. The Nb–O–Ti bonds and defects at cation sites are considered key factors for increasing the transformation temperatures for conversion of the nanosheets to anatase and finally into rutile. It is further tempting to link the delay in crystallization to morphology limitations originating from the nanosheets. The present work shows that layered Nb-titanates are appropriate precursors for formation of highly oriented Nb-substituted anatase thin films via delamination, reconstruction and subsequent heat treatment.

1. Introduction

Layered titanates with lepidocrocite (γ-FeOOH)-type structure attracts attention due to prominent photocatalytic activity [1,2] and interlayer chemistry [3,4]. Layered alkali metal titanates like $Cs_{0.70}Ti_{1.825}\square_{0.175}O_4$ (□ = vacancy) are composed of negatively charged host layers of edge-shared TiO_6-octahedra compensated by interlayer cesium ions [5]. Ion-exchange/intercalation properties of substituted titanates $A_xTi_{2-x/2}M_{x/2}O_4$ (A = Cs, K, Rb; M = Mg, Fe, Co, Ni, Cu, Zn) have been extensively studied [5–10]. Some of these are unstable upon acidic treatment, e.g. in the case of Li-/Mg-substituted variants, both these ions in the host layers and interlayer cesium get completely extracted during an acidic exchange process [10].

Recently we reported a novel sol–gel assisted solid-state reaction (SASSR) route for production of phase-pure layered Nb-substituted titanates $Cs_{0.70}Ti_{1.8.25-x}Nb_xO_4$ [11], in which the Ti^{IV} is partially substituted by Nb^V in the host layers. The SASSR route enables synthesis of Nb-substituted titanates for subsequent exfoliation and opens hence up for design of Nb-substituted TiO_2 films and particles. This soft chemistry route may provide products with significant differences with respect to morphology, substitution level and homogeneity, as well extending the thermal stability window of metastable anatase. Physical properties are polymorph dependent. Furubayashi et al. [12] reported that PLD grown anatase films, a-$Ti_{1-y}Nb_yO_2$, $y \approx 0.03$ show prominent electric and optic properties quite comparable with ITO (In–Sn_2O_3). On the other hand, rutile type films possess high resistivity with no potential as transparent conductive oxides (TCO) [13].

Although intensively studied, important questions remain open for the layered titanates as precursors for chemically modified anatase (a-) and rutile (r-) materials. One critical aspect is whether the higher-valent Nb^V-substituent remains stable within the layered precursor upon ion-exchange or will leach out as observed for Li- and Mg-substitution. A second aspect is whether such substitution may help stabilizing the anatase polymorph owing to structural similarities with the layered precursor, possibly in combination with aspects of defects, growth mechanisms and morphology, and thereby adding to the

* Corresponding author at: Materials Research Division, Risø National Laboratory for Sustainable Energy, Technical University of Denmark, P.O.Box 49, DK-4000 Roskilde, Denmark.
E-mail address: pnor@risoe.dtu.dk (P. Norby).

0022-4596/$ - see front matter © 2011 Elsevier Inc. All rights reserved.
doi:10.1016/j.jssc.2011.08.039

well-known relationship between particle size and TiO_2 polymorphism with anatase favored for sizes <11 nm, brookite for 11–35 nm and rutile for sizes >35 nm [14]. The possibility to tune oxidation state, defects, structure and morphology by Nb-substitution, may provide means to optimize the physical response of such particles and films, e.g. for application and as TCO. Further critical aspects concerns the chemical homogeneity at the local scale as well as the resulting electronic properties of the solid solution phases. Here soft chemistry offers additional possibilities to those of high temperature ceramic routes.

The present study addresses these key questions through a series of systematic studies on delamination, reconstruction, and subsequent post treatments aiming at $(Nb,Ti)O_2$ samples in the form of powders and sprayed materials. This includes studies of ceramic model materials of NbO_2–TiO_2 (and oxidized variants) with respect to local and average structure, and to electronic properties. Results are discussed on the basis of (synchrotron) XRD, AFM, TGA, SEM, XPS, ^{93}Nb MAS NMR, magnetic and electric transport studies.

2. Experimental section

2.1. Exfoliation, ultrasonication, and restacking of nanosheets

As-synthesized layered titanates, $Cs_{0.70}Ti_{1.825-x}Nb_x\square_{0.175}O_4$ ($x=0$–0.03) and proton-exchanged $H_{0.70}Ti_{1.825-x}Nb_xO_4\cdot nH_2O$ ($x=0$–0.03) were prepared as described in Ref. [11]. Niobium is introduced to the formula without changing the oxygen or cation stoichiometry. As Nb enters with a valence of five, the cation stoichiometry is likely to change in order to keep overall charge neutrality. A correct structure-chemical formula would require information on defect chemistry. We hence adopt a simplified notation and assume that the Cs-content remains unaffected (since observed interlayer changes are very small). Note, the Cs-content is reflected in the concentration of vacancies at the octahedral Ti-site; i.e. $Cs_zTi_{2-z/4}\square_{z/4}O_4$. For the current samples with $z=0.70$, we thus obtain $Cs_{0.70}Ti_{1.825}\square_{0.175}O_4$, and abbreviate the formula $Cs_{0.70}Ti_{1.825-5x/4}\ Nb_x\square_{0.175+x/4}O_4$ for the Nb-substituted samples as $Cs_{0.70}Ti_{1.825-x}Nb_xO_4$.

$H_{0.70}Ti_{1.825-x}Nb_xO_4\cdot nH_2O$ ($x=0$–0.03) was exfoliated in an aqueous solution of tetrabutylammonium hydroxide (TBAOH, 5 wt%) by dispersing 100 mg ion-exchanged powder into 100 ml TBAOH at 40 °C for 10 d under constant stirring. The colloid product was separated by centrifugation at 15,000g for 15 min. Thereafter, TBA-titanate nanosheets were obtained by dispersing the colloid product in water. The stable suspensions of exfoliated Nb-titanates were restacked by freeze-drying; yielding a voluminous white solid with a cotton-like appearance (termed restacked material).

The effect of ultrasonication on delamination with respect to size and shape of nanosheets were studied for suspensions treated in an ultrasonic bath (Bransonic 2510E –DTH; 100 W, 42 kHz $\pm$ 6%) in four sequences of each 30 min with 60 min pauses to avoid heating. The turbidity, in nephelometric turbidity units (NTU), was measured after each treatment using a Merck Turbiquant 3000 IR turbidimeter.

2.2. Heat treatment of TBA-precursors and synthesis of model materials

Phase transformations and thermal stability of TBA-intercalated titanates were studied by *in situ* high temperature (HT) X-ray diffraction between room temperature and 500 °C. Small batches of restacked TBA-layered titanates were furthermore annealed at temperatures from 500 to 900 °C in air for 2 h, thereafter cooled to ambient and analyzed with respect to phase content and morphology. Selected sets of restacked samples were heated in reducing atmosphere (ca. 10% H_2 in Ar) for 12 h at 700 and 1000 °C, subsequent to a first calcination at 500 °C in air for 12 h.

Ceramic model materials for studies of the rutile type $Ti_{1-y}Nb_yO_2$ solid solution ($0\le y\le 0.30$) with respect to structure and electronic properties were prepared from weighed amounts of TiO_2 (99.8%, from Aldrich) and NbO_2 (99.99%, from Aldrich), mixed in ethanol and ground in an agate mortar. The ethanol was removed by heating at 200 °C for 2 h before pelletizing. The pellets were subjected to two different heat treatments. In treatment A they were heated in an evacuated silica tube at 1100 °C for 5 d. Some pellets were thereafter heated in air at 900 °C for 24 h (treatment B). Pellets of pure TiO_2 were treated similarly and served as reference.

To better describe the various $Ti(Nb)O_2$ materials, the ceramic model materials are denoted as C–$Ti_{1-y}Nb_yO_2$ ($0\le y\le 0.30$), and the materials from layered precursors as L–$Ti_{1-y}Nb_yO_2$ ($0\le y\le 0.0164$). The relationship between the substitution level x in $Cs_{0.70}Ti_{1.825-x}Nb_x\square_{0.175}O_4$ and y in $Ti_{1-y}Nb_yO_2$ is $y=x/1.825$.

2.3. Fabrication of thin films from exfoliated nanosheets

Nb-substituted films were obtained by a twin-fluid spray pyrolysis system, having a distance between nozzle and substrate of 2.5 cm. Spraying of a 0.1 g/L exfoliated TBA-precursor solution at a flow rate of 3.0 ml/min was achieved at N_2 pressure of 0.25 atm. Cleaned silicon wafers, Si(1 1 1) and Si(1 0 0), were used as substrate. The temperature of the substrate during the 3 min depositions was 300 °C. The as-prepared samples were thereafter heated at 700 °C for 5 h in air using a ramp rate of 5 °C/min.

2.4. Characterization

Phase analyses were carried out by powder X-ray diffraction (XRD), using Siemens D5000 powder diffractometers in reflection and transmission (capillary) geometry (Cu $K\alpha_1$ radiation; Braun positional sensitive detector). High temperature XRD data were collected between 25 and 500 °C by heating the samples in 0.5 mm quartz glass capillaries at a rate of 0.5 °C/min by means of hot air from a heating gun ($2\theta=3$–60°; step size 0.015°; time per step 0.5 s). High resolution synchrotron powder X-ray diffraction data were collected between $2\theta=0.5190$ and 37.992° at ID31, ESRF, wavelength $\lambda=0.39987$ Å, using borosilicate capillaries of 0.7 mm diameter. 12,492 data points entered into the Rietveld refinements of the Fullprof program, giving $R_{wp}=9.2$ ($R_{exp}=7.4$). The background was described with a 12-terms polynomial function and peak shape by pseudo-Voigt and asymmetry functions.

Sample morphology was analyzed by scanning electron microscopy (SEM, FEI Quanta 200 F, operated at an accelerating voltage of 30 kV). Chemical analysis was performed by Inductively Coupled Plasma-Atomic Emission Spectroscopy (Vista Ax. CCD Simultaneous ICP-AES). Thermogravimetric analysis (TGA) was performed on a Perkin-Elmer TGA 7 system in nitrogen atmosphere at a heating rate of 10 °C/min.

Atomic Force Microscopy (AFM) images were obtained on a Nanoscope E multimode AFM (Digital Instruments) operated in tapping mode in air at room temperature. One drop of the clear dispersion of exfoliated nanosheets in water (0.02 g/L) was dripped onto a freshly cleaved and smooth mica surface (1×2 cm^2; average roughness ca. 0.1 nm) and conditioned at room temperature for 24 h.

Magnetic properties were investigated using a Physical Property Measurement System (Quantum Design: PPMS Model-6000). Dc-magnetization data were collected by the dc-extraction method in both zero-field-cooled (ZFC) and field-cooled (FC)

modes under a magnetic field, $H=5000$ Oe for $10\ K \le T \le 270\ K$ in sweep mode of 2 K/min. Electric transport property was measured using a standard four-probe measurement apparatus (Quantum Design: PPMS Model-6000) to avoid errors owing to surface resistance.

XPS data were collected on a KRATOS AXIS ULTRA^{DLD} using Al $K\alpha$ radiation. Charge neutralization was accomplished via low kinetic energy electrons. The C 1*s* peak was fixed at 284.8 eV in the evaluation of binding energies for peaks in the survey and high resolution spectra.

^{93}Nb NMR data were collected on a Bruker Avance III 500 MHz spectrometer operating at a frequency of 122.413 MHz. The spectra were obtained using a 3.2 mm MAS probe spinning at a rate of 20 kHz. The chemical shifts of ^{93}Nb were externally referenced to a saturated $NbCl_5$ in acetonitrile solution. The spectra were obtained using 0.5 μs pulses at a 125 kHz rf-field with a recycle delay of 2 s. Either 12288 or 24576 transients were used to obtain spectra.

3. Results and discussion

3.1. Properties of dense and layered Nb-substituted titanates

The observed change in unit cell dimensions of as-synthesized layered $Cs_{0.70}Ti_{1.825-x}Nb_xO_4$ ($0 \le x \le 0.03$) and its derived proton-exchanged form as function of Nb-content (x), proves that Nb is incorporated into the titanate host layers [11]. The main change occurs for the longer *b*-axis which corresponds to the stacking direction. The ionic radius for Nb^V is just slightly larger than for Ti^{IV} with coordination number six. This is consistent with the rather constant values for the *a*- and *c*-axes. As Nb enters with a valence of five, the cation stoichiometry is likely to change in order to keep overall charge neutrality. There are several ways in which the Nb substitution could be compensated, including an increase in vacancies or decrease in the Cs content. Clarification would require studies beyond the scope of the present work.

The compositions before and after proton exchange of layered $Cs_{0.70}Ti_{1.825-x}Nb_xO_4$ were determined by ICP-AES, see Table 1. More than 99% extraction of the cesium ions was achieved after three cycles of H^+ ion-exchange. The accuracy of the ICP analysis is, however, not sufficient to conclude on any correlation between Cs- and Nb-contents. It is important to notice that the Nb^V-substituent introduced to the host layers is not extracted even after three cycles of proton exchange. We currently observed a quite parallel situation with respect to changes in unit cell dimensions and leaching stability for W-substituted layered precursors (no further data included). It hence appears facile to achieve higher valent substitutions for Ti^{IV} into the TiO_2 polymorphs by the use of layered precursors. This could indeed prove advantageous for stabilizing the anatase polymorph, since higher valent substituents have been reported to retard the temperature induced transformation into rutile [14]. Lower valent (e.g. Li or Mg) substituted materials, on the other hand, become unattainable due to leaching of host layer cations, see above. With respect to possible practical applications it is essential that well-defined materials can be obtained. In this respect, Nb- and W-substituted titanates appear promising.

Table 1
Results from ICP-AES analyses of $Cs_{0.70}Ti_{1.825-x}Nb_xO_4$ and their proton exchanged forms.

Compounds	Targeted molar ratios		Molar ratios determined by ICP-AES	
	Cs/Ti	Nb/Ti	Cs/Ti	Nb/Ti
$Cs_{0.70}Ti_{1.825-x}Nb_xO_4$				
$x=0.02$	0.390	0.011	0.400	0.010
$x=0.03$	0.390	0.017	0.390	0.017
$H_{0.70}Ti_{1.825-x}Nb_xO_4yH_2O$				
$x=0.02$	0.000	0.011	0.000	0.012
$x=0.03$	0.000	0.017	0.000	0.016

Conversion into dense polymorphs was achieved by freeze-drying of the colloidal TBA-titanates, calcination and heat treatment at 700 or 1000 °C in either air or H_2, see Section 2. In all cases slightly expanded unit cells of the anatase and rutile polymorphs of L–$Ti_{1-y}Nb_yO_2$ were observed, Fig. 1. This proves that Nb enters as a solid solution substituent.

For a given Nb-content, the unit cell volume expansion is less for samples heated in air than in H_2. For the H_2 treated samples the volume increases linearly over the studied concentration range whereas for air treated rutile type L–$Ti_{1-y}Nb_yO_2$ the unit cell volumes take constant values for $y=0.0110$ and 0.0164 (i.e. $x=0.02$ and 0.03 for the layered precursors). The C–$Ti_{1-y}Nb_yO_2$ model materials made by the ceramic route in sealed, evacuated silica ampoules, cover a much larger composition range. The unit cell volumes are shown in Fig. 2 for $y \le 0.30$. The unit cell volume $V(y)$ varies approximately linearly with y. This agrees well with earlier findings and is fairly consistent with our results for the thermally converted titanates (with $y < 0.02$). However, the unit cell volume of the layered precursor based materials is somewhat larger, e.g. 62.73 Å^3 observed while 62.57 Å^3 expected for $y=0.0164$ on the basis of the model samples. It is tempting to correlate the expanded volume with the synthesis route and suggest this to be caused by differences in chemistry (e.g. local structure, oxidation states, defects, etc.).

The C–$Ti_{1-y}Nb_yO_2$ model samples treated in air at 1100 °C has a solubility limit of $y=0.10 \pm 0.01$ as indicated by the flattening out of $V(y)$, Fig. 2, and by the appearance of $TiNb_2O_7$ impurities in the XRD patterns. The observed volume expansion is in accordance with [15], however, the current solubility limit of some 0.10 is higher than the earlier reported value of 0.07. Fig. 2 reveals differences in volumes between oxidized (Ti^{IV}; Nb^V) and reduced C–$Ti_{1-y}Nb_yO_2$ ($y < 0.10$). This may indicate a possibility to achieve intermediate compositions (partly reduced samples) given that appropriate heat treatments are being applied, which could open for a new route towards tuning of physical properties in these systems.

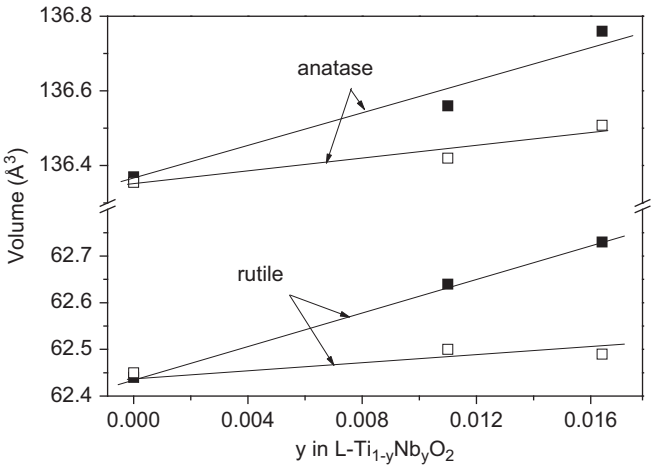

Fig. 1. Unit cell volumes of anatase and rutile L–$Ti_{1-y}Nb_yO_2$ formed from layered precursors as a function of Nb content (y). ■, heated in reducing atmosphere; □, heated in air.

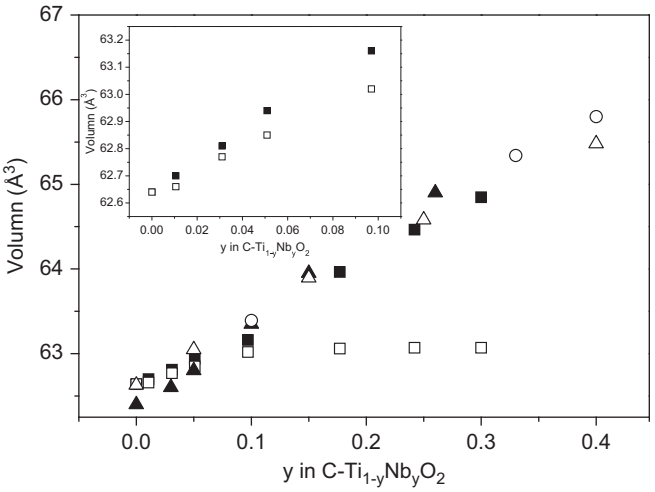

Fig. 2. Unit cell volumes of ceramically synthesized C-$Ti_{1-y}Nb_yO_2$ as a function of Nb content. Insert presenting data for samples with $y < 0.1$. ■, heated in vacuum; □, heated in air;▲, from Ref. 15, heated in vacuum; Δ, from Ref. 16, heated in vacuum and ○ is from Ref. 17, heated in a reducing atmosphere (CO/CO_2 in the ratio of 1/20).

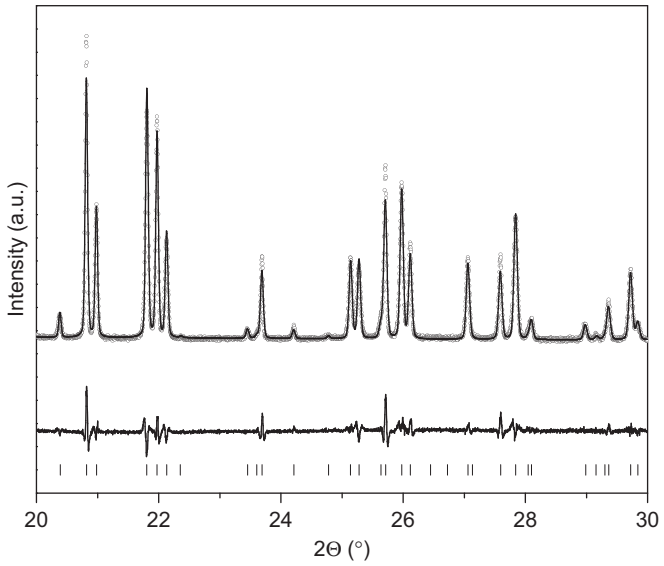

Fig. 3. Selected part of the synchrotron XRD intensity profiles for C–$Ti_{0.7}Nb_{0.3}O_2$. $\lambda = 0.39987$ Å. Observed points (open circles), calculated profiles (full line), difference plot (lower full line) and positions for reflections (vertical bars).

The high resolution powder synchrotron diffraction data for $y = 0.30$, Fig. 3, are fully consistent with a substitutional solid solution phase for C–$Ti_{1-y}Nb_yO_2$ [15,16] and excludes any impurities or deviations from the average $P4_2/mnm$ model; $a = 4.6599(1)$, $c = 2.9888(1)$Å; (Ti,Nb) in 2*a*; O in 4*e* Wückoff sites. The Rietveld refinements gave $x_O = 0.3024(2)$, and a relative site occupancy of 30.4(4)% Nb at the cation sites. The average (Ti,Nb)–O distance of the $(Ti,Nb)O_6$-octahedron was found to be 1.986 Å for $y = 0.30$ which is in good accordance with prevailing neutron data [17] and expectations based on size variations as function of oxidation state of Ti and Nb.

Regarding electronic states, earlier studies have suggested a complex charge situation upon formal Nb^{IV} introduction into r-TiO_2; i.e. formation of Ti^{III} and Nb^{V}. Present XPS data confirms this suggestion. As revealed from Fig. 4a, a clear shoulder indicative of Ti^{III} appears at the low energy side of the Ti^{IV} $2p_{3/2}$ peak in the XPS spectra. For niobium no shoulder could be observed for the $3d_{5/2}$ peak and the Nb-signal is hence fully consistent with Nb^{V} (Fig. 4b). The solid solution can hence be described as C–$Ti^{IV}_{1-2y}Ti^{III}_yNb^{V}_yO_2$. The oxidized phase is described correspondingly as C-$Ti^{IV}_{1-5y}\square_yNb^{V}_{4y}O_2$ (□ vacancy).

Independent of the description, d^1 species (Ti^{III} or Nb^{IV}) prevail, and the solid would be paramagnetic. This was confirmed by magnetic susceptibility measurements, consistent with the changed color of the sample. The susceptibility data in Fig. 5 show a weak anomaly around 60 K, unlikely to reflect long range magnetic order. We tentatively suggest a change in electronic states of the involved Ti- and Nb-species. Based on the ionic model from XPS, C–$Ti^{IV}_{1-2y}Ti^{III}_yNb^{V}_yO_2$, the calculated $\mu_{eff}(total) = 0.55\ \mu_B$ is in accordance with the observed value of 0.6 μ_B for $y = 0.1$. Transport property data indicate semiconducting behavior with poor conductivity at low Nb-substitution levels (insert to Fig. 5). Resistivity data above some 200 K satisfy the Boltzman equation and yield activation energies of 0.06–0.1 eV. The Nb-substituted rutile is in accordance with literature not a TCO candidate.

The L–$Ti_{1-y}Nb_yO_2$ obtained by thermal transformation of layered Nb-substituted titanates ought to exhibit the same key features as the model materials. One critical issue concerns the distribution of niobium within the TiO_2 matrix; with possibilities ranging from random solid solution, via clustering to nanocomposites with Nb_2O_5 precipitates rather than solid miscibility. The low Nb-concentrations in these transformed materials make studies difficult. The volume expansion upon substitution, Fig. 1, renders no doubt that bulk substitution is taking place. The current ^{93}Nb MAS-NMR data provide independent evidence, see spectra in Fig. 6. The spectra for the reduced samples are poor, consistent with the prevailing paramagnetism, and show notably no indication for Nb_2O_5. Important insight was provided by the diamagnetic samples. Although the first coordination is octahedral for Nb in both Nb_2O_5 and $(Ti,Nb)O_2$, the next nearest neighbors are different, respectively, Nb and predominantly Ti atoms. First, Nb_2O_5 has clear signatures in the ^{93}Nb spectrum, Fig. 6a. These signatures are also observed for oxidized model samples outside the solid solution range, i.e. with $y > 0.10$ (Fig. 6c, d), confirming their two-phase nature. The ^{93}Nb spectra for the oxidized $(Ti,Nb)O_2$ ceramic solid solution samples and the oxidized converted (layered) materials show strong similarities, Fig. 6b and e. In both these solid solution samples the lack of the signatures of Nb_2O_5 clearly indicates the absence of (nano)-precipitates of Nb_2O_5 at outer surfaces and grain boundaries. Therefore, on the basis of the XRD, XPS and ^{93}Nb MAS NMR data one can conclude that the soft chemical approach provide products with niobium cations finely dispersed into the TiO_2 matrix, i.e. reduced and oxidized Nb-doped TiO_2 (anatase and rutile) can successfully be achieved from layered precursors via ion exchange, exfoliation, and calcination.

3.2. Exfoliation and effect of ultrasonic treatment on nanosheets

The protonated layered titanate $H_{0.70}Ti_{1.825-x}Nb_xO_4 \cdot nH_2O$, $0.00 \le x \le 0.03$, is readily exfoliated into single nanosheets with 2D morphology by exchanging the interlayer H_3O^+ ions with bulky organic amine cations in water solution. An AFM image of the exfoliated titanate TBA–$Ti_{1.825-x}Nb_xO_4$ ($x = 0.02$) is shown in Fig. 7a. The individual exfoliated nanosheets have an average thickness of 1.0 nm and show no sign of stacking or aggregation. The average surface roughness is 0.06 nm, see Table 2, and is within the roughness scale of the support.

Ultrasonication treatment promotes exfoliation of layered materials such as LDH [18] and titanates [19]. Changes in morphology and size of nanosheets may follow upon prolonged exposure to ultrasonication [20]. The turbidity of the dispersions of TBA-intercalated materials provides indirect information on

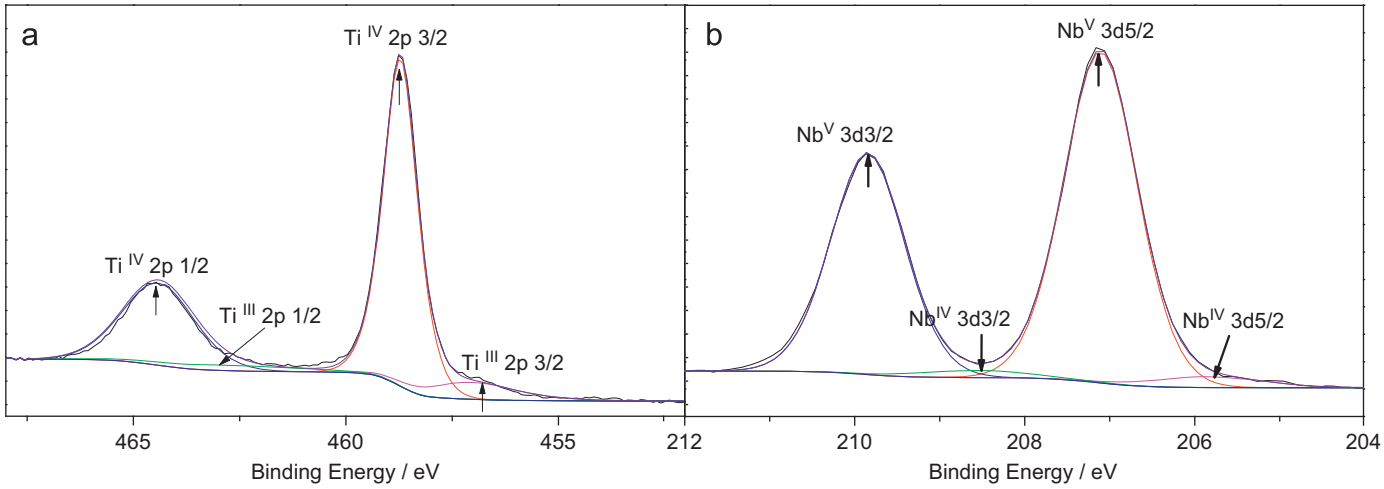

Fig. 4. (a) Ti 2*p* and (b) Nb 3*d* XPS of C–$Ti_{0.9}Nb_{0.1}O_2$ model sample heat-treated at 1000 °C in H_2.

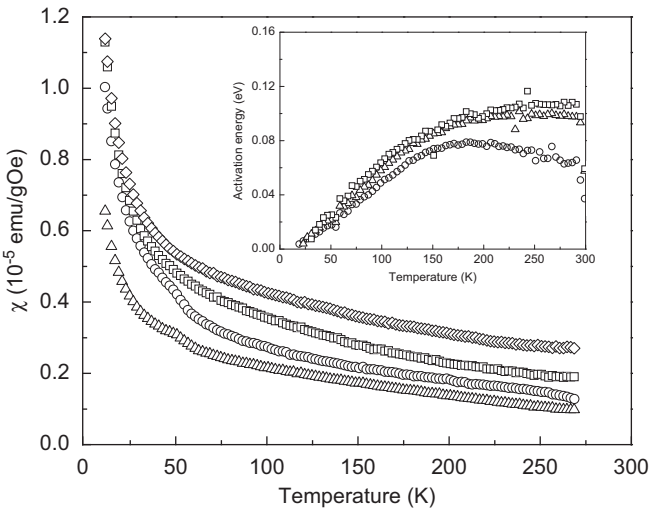

Fig. 5. Magnetic moment of ceramic model samples C–$Ti_{1-y}Nb_yO_2$, y=0.1(○); 0.18 (Δ); 0.24 (□) and 0.3 (◇), H= 5000 Oe. Insert is the activation energies of model samples at different temperatures.

the nanosheet morphology. At higher particle concentrations (1.0 and 0.5 g/L), the turbidity decreases fast due to two combined effects; exfoliation of the TBA-material and cracking of nanosheets before leveling out to nearly constant values (75 and 45 NTU, respectively). At lower concentrations, 0.1 and 0.02 g/L, the decrease is less pronounced and the turbidity stabilizes around 35 and 15 NTU, respectively. At low concentration (0.02 g/L) the TBA-material exfoliates readily into single layer nanosheets in water even without ultrasonic treatment, Fig. 7a. Thus, the decrease of turbidity during sonication of such samples may reflect fragmentation of the larger nanosheets and a reduction in the average sheet size to around 10% of the original ones, Fig. 7a–e and Table 2. Notably, the turbidity increases when suspensions become more concentrated with particles (see above). However, the stable turbidity levels observed after long sonication (600 min) are not directly proportional to the initial TBA-material concentrations. This indicates that the nanosheet size is contributing more to the turbidity than does the number of particles.

Interestingly, the nanosheets become corrugated when sonicated for more than 60 min. The distance between the resulting ripples is ca. 30 nm (Fig. 7e). The average roughness increases due to the corrugation (Table 2). The line profile shows that the average nanosheet thickness is maintained at 1.0 nm, Fig. 7f. For highly concentrated dispersions ultrasonication is found to accelerate exfoliation. Both cracking and corrugation result in smaller nanosheets and reduced turbidity.

3.3. Properties of restacked materials and thermal transformations

Restacked exfoliated nanosheets obtained by freeze-drying of the colloidal suspension were used as solid precursors for thermal transformations into anatase and rutile. Of interest is to clarify whether Nb-substitution in the layered precursor may help stabilizing the anatase polymorph owing to structural similarities, as consequence of morphology, or due to reduced transformation rate as claimed to result from the a low number of oxygen defects for materials with higher valent substituents [14].

The room temperature XRD patterns (capillary geometry) of the restacked TBA- materials (Fig. 8a) show well-defined basal plane diffraction peaks. The reflections at 2θ=4.9°, 9.9° and 15.0° are indexed as (0 k 0), k=2, 4, 6, assuming $b \approx 3.5$ nm, and prove the presence of a lamellar structure with interlayer separation 1.75 nm [20]. The (2 0 0) at 2θ=48.2°, d=0.189 nm, shows that a lepidocrocite type atomic arrangement is likely maintained within the layers. The broad and asymmetric (1 3 0) at 2θ=25.5° indicates significant disorder in the restacked material (Fig. 8b).

The SEM image, Fig. 8c, of the restacked material reveals a sheet-like morphology of particles with a lateral size up to tens of micrometers. These studies further indicate a particle thickness of 50–100 nm, which suggests that the restacked flakes consist of 30–60 layers of nanosheets.

The thermal transformations were investigated by *ex situ* and *in situ* HT-XRD, see Fig. 9. Similar transformation schemes were observed for all samples. The stepwise shift in the position of (0 2 0) of restacked TBA–$Ti_{1.825-x}Nb_xO_4$ towards higher diffraction angles upon heating, Fig. 10, indicates significant changes in interlayer chemistry. Between RT and 130 °C (step 1) the interlayer separation remains unchanged yet thermogravimetric analysis (insert to Fig. 10) shows 4 wt% mass loss, probably due to loss of interlayer water. This stems probably from remaining H_3O^+ due to non-complete TBA-ion exchange. The water loss does not affect the interlayer separation which is ruled by the size of the TBA-ions. The abrupt change at 150 °C in the interlayer spacing of 0.2–0.3 nm (step 2) is probably due to rearrangement and partial breakdown of the TBA-ion as indicated by the TGA

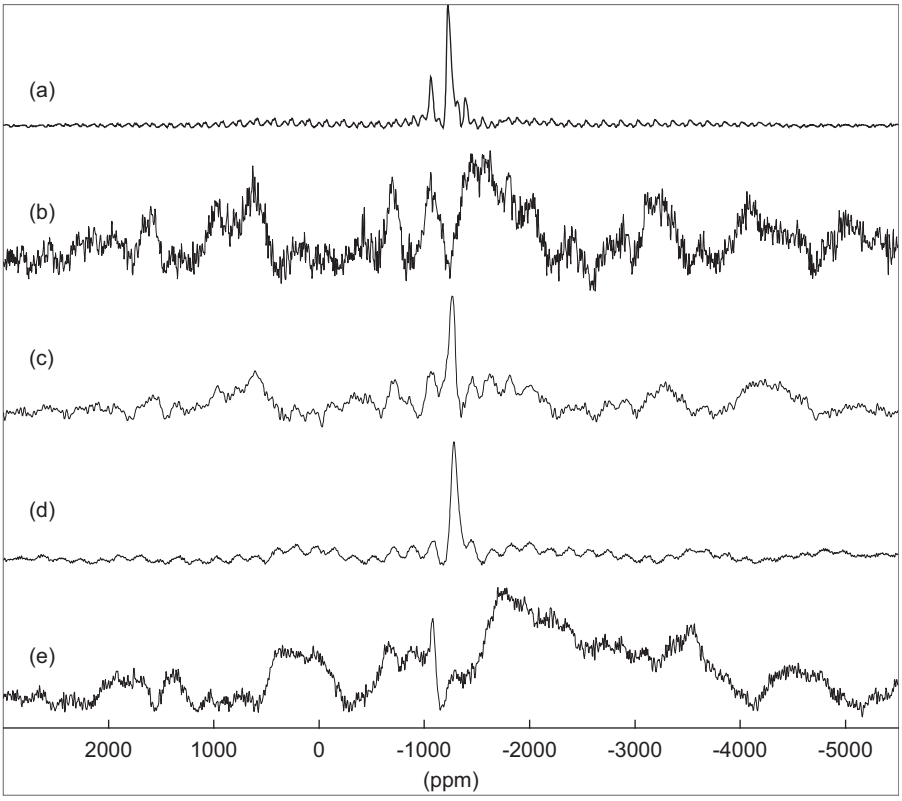

Fig. 6. ^{93}Nb NMR spectra of (a) Nb_2O_5; oxidized model samples: C–$Ti_{1-y}Nb_yO_2$, (b) $y=0.05$, (c) $y=0.1$, (d) $y=0.2$; oxidized converted (layered) material: (e) L–$Ti_{1-y}Nb_yO_2$, $y=0.016$.

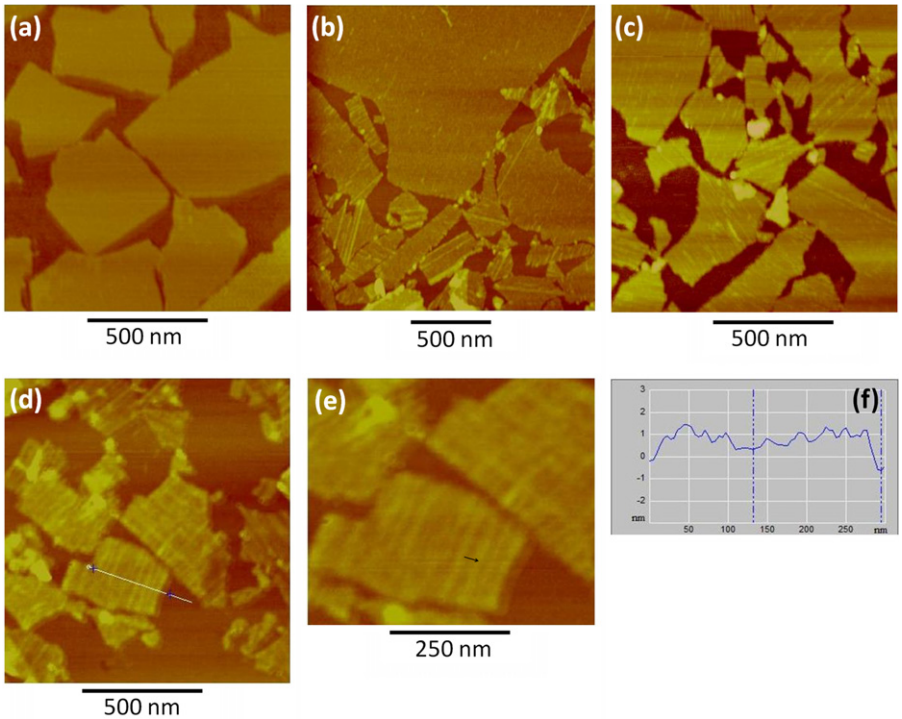

Fig. 7. AFM tapping mode images of exfoliated TBA–$Ti_{1.825-x}Nb_xO_4$ ($x=0.02$; 0.02 g/L) as function of ultrasonication time: (a) 0 min; (b) 30 min; (c) 60 min and (d) 600 min, (e) is the magnified image of (d), the black arrow indicates the distance between ripples is ca. 30 nm. (f) is a line profile of (d).

loss. At 260 °C (step 3) a second drop in the spacing of ~0.4 nm is associated with a weight loss of 15 wt%, probably reflecting decomposition of TBA.

The *in situ* XRD data, Fig. 9a, show that the layered precursor still remains at 300 °C, though Bragg reflections now being very broad. As mentioned, the (2 0 0) at $2\theta \sim 48^\circ$ suggests that a

Table 2
Results from AFM particle size analysis of exfoliated titanate ($x=0.02$; 0.02 g/L) as a function of ultrasonication time.

Ultrasonication time (min)	Size of nanosheets[a] (μm^2)	Average height[a] (nm)	Average roughness of single layer surface[a]—R_a (nm)
0	0.54	1.00	0.06
30	0.31	1.00	0.10
60	0.15	1.00	0.16
600	0.06	1.00	0.23

[a] Size of the nanosheets are the average data calculated from a much larger area ($5\times5\ \mu m^2$). The average thickness and roughness of the nanosheets were obtained from the section analysis and the selected areas in the AFM images (Fig. 4), respectively.

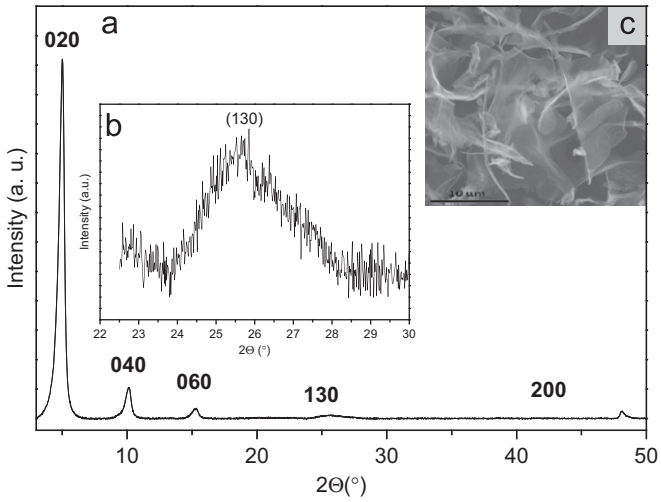

Fig. 8. XRD pattern of (a) the restacked sample TBA–$Ti_{1.825-x}Nb_xO_4$ ($x=0.02$) collected in transmission geometry. The insert (b) is a close-up of the 130 peak ($22.5\le2\theta\le30$). Inset (c) is the SEM image of the sample.

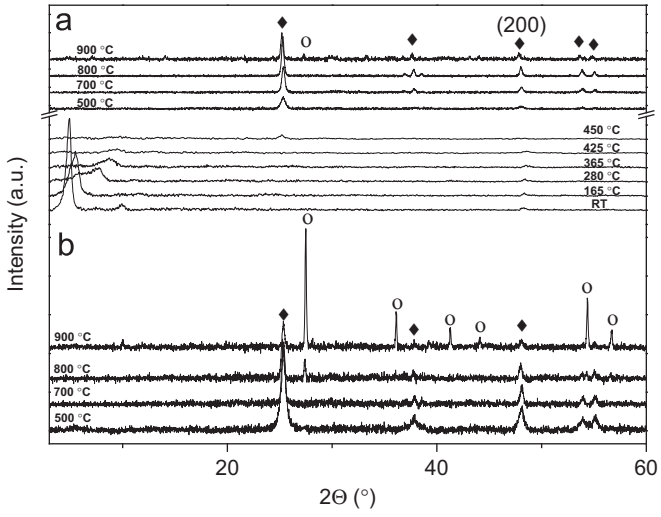

Fig. 9. (a) *In situ* HT-XRD and *ex situ* XRD patterns of TBA–$Ti_{1.825-x}Nb_xO_4$, $x=0.03$; (b) is *ex situ* XRD patterns of TBA-$Ti_{1.825}O_4$. Data for $T\le450$ °C were collected *in situ*, for 500–900 °C were collected *ex situ*. ♦, anatase; ○, rutile.

lepidocrocite like atomic arrangement prevails within the layers. Further heating results in an amorphous product before an anatase type phase is formed around 400 °C for $x=0.00$ (not presented in Fig. 9), consistent with expectations for a 30–60

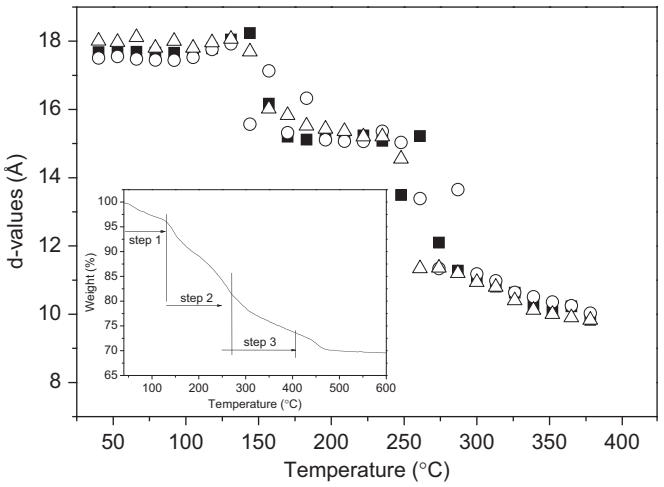

Fig. 10. d-Values of (020) of restacked TBA–$Ti_{1.825-x}Nb_xO_4$ samples versus temperature, $x=0$ (■); $x=0.02$ (○) and $x=0.03$ (Δ). The insert shows TGA data of TBA–$Ti_{1.825-x}Nb_xO_4$ ($x=0.02$).

Table 3
Relative amounts of anatase and rutile calculated from XRD data using an empirical equation[a].

Temperatures (°C)	(TBA–)$Ti_{1.825}O_4$ ($x=0$)		(TBA–)$Ti_{1.825-x}Nb_xO_4$ ($x=0.02$)		(TBA–)$Ti_{1.825-x}Nb_xO_4$ ($x=0.03$)	
	Anatase (%)	Rutile (%)	Anatase (%)	Rutile (%)	Anatase (%)	Rutile (%)
500	100	0	100	0	100	0
700	100	0	100	0	100	0
800	58	42	76	24	100	0
900	13	87	49	51	79	21

[a] $\left(\frac{\text{Rutile}}{TiO_2}\right)_{RX}=1.369\frac{I_R}{I_A+I_R}-0.369\left[\frac{I_R}{I_A+I_R}\right]^2$

where I_R is the intensity of (110) rutile reflection and I_A is the intensity of (101) anatase reflection.

layer thick material, see SEM above and [21]. For $x=0.03$ the transformation temperature is increased to 450 °C. The observed increase in transformation temperature from 400 °C for $x=0.00$ to 450 °C for $x=0.03$ is likely related to the Nb substitution. [14]. Close to the transformation, very broad anatase peaks are observed, indicating strained and/or nm-sized particles. Furthermore, the presence of the 200 reflection ($2\theta=48.2°$) right up to the transformation into anatase, suggests that the nanolayers remain intact, while the integrity of the stacking is lost prior to the transformation. It is tempting to link the delayed crystallization to morphology limitations originating from the nanosheets [14]. Note that anatase normally will crystallize to rutile at 400 °C if no other factors are in play [14]. It is reported [21] that shortage of component atoms to construct the anatase may inhibit crystallization at normal temperatures. Both nucleation and growth of anatase from the nanosheets would require thermal activation and atomic diffusion. Strong Nb–O–Ti bonds in the nanosheets may hinder transport of Ti atoms to initiate nucleation, although the restacked nanosheets (>5 layers) contain sufficient Ti and O atoms to produce some unit cells of anatase.

The effect of thermal treatment on restacked samples at temperatures ≥500 °C were studied *ex situ* by means of XRD at room temperature, see Fig. 9. For $x=0.00$ anatase- and rutile-like phases coexist at 800 °C (9b). At 900 °C the phase conversion from anatase to rutile is almost complete; 87% being rutile according to

quantitative X-ray analysis, see Table 3. For $x=0.03$, the anatase phase remain the sole crystalline phase even at 800 °C (2 h annealing), Fig. 9a. A small amount (21%) of a rutile-like phase appears at 900 °C after 2 h heating. This indicates that Nb^V-substitution into the titania nanosheets suppresses the phase conversion to rutile which is in line with the observed crystallization of anatase. Note in this respect that the transformation between the anatase and rutile polymorphs is reconstructive and involves nucleation and growth. Hence, the dispersed Nb-cations introduced upon substitution appear to modify the defect situation of anatase and inhibit the phase transformation by slowing down the growth of nuclei above the critical size [14]. A corresponding perturbation of the transformation behavior in the range of 600–700 °C is reported for Nb-substituted titania nanoparticles [22,23]. However, since the transformation temperature of 900 °C for the nanosheets is significantly higher than for the mentioned nanoparticles, one may speculate whether also morphology influences the recrystallization [14].

The SEM images of restacked samples heated at 500 and 900 °C for 2 h in Fig. 11 show that the calcined samples retain flake-like morphology. Granular crystallites at the edge of nanosheets heated at 900 °C indicate recrystallization and likely

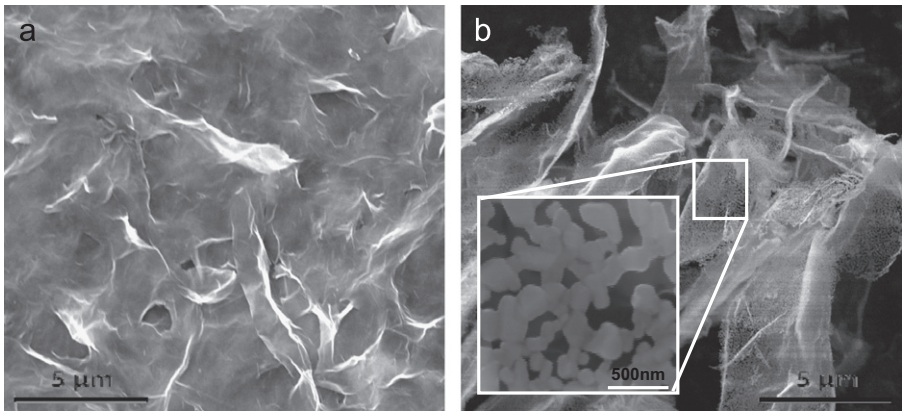

Fig. 11. SEM images of restacked TBA–$Ti_{1.825-x}Nb_xO_4$, $x=0.02$ heated at (a) 500 °C and (b) 900 °C for 2 h in air.

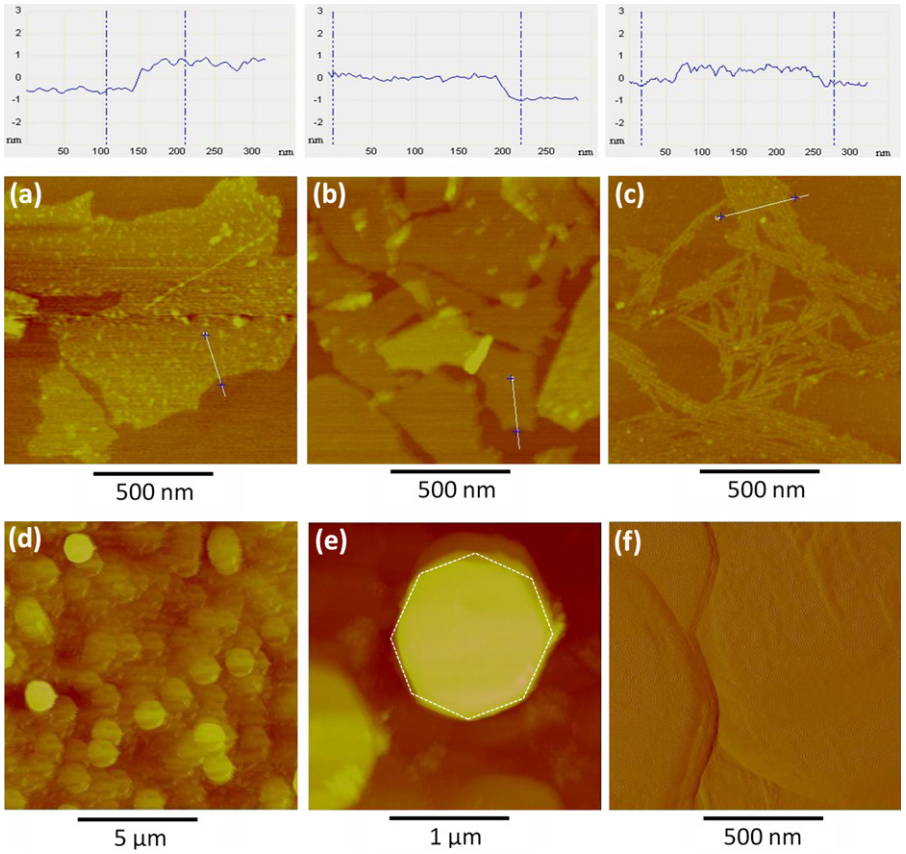

Fig. 12. AFM tapping mode images of restacked TBA–$Ti_{1.825-x}Nb_xO_4$ ($x=0.02$) heated at 300 (a), 500 (b), and 900 °C (c) for 2 h. Line section analyses are shown above the images. (d) AFM tapping mode image of $Ti_{1.825-x}Nb_xO_4$, $x=0.03$ thin film fabricated by hot spray on Si (1 1 1) for 3 min and heated at 700 °C in air for 5 h; (e) zoom of a single sheet in image (d); (f) amplification of selected area of image (d).

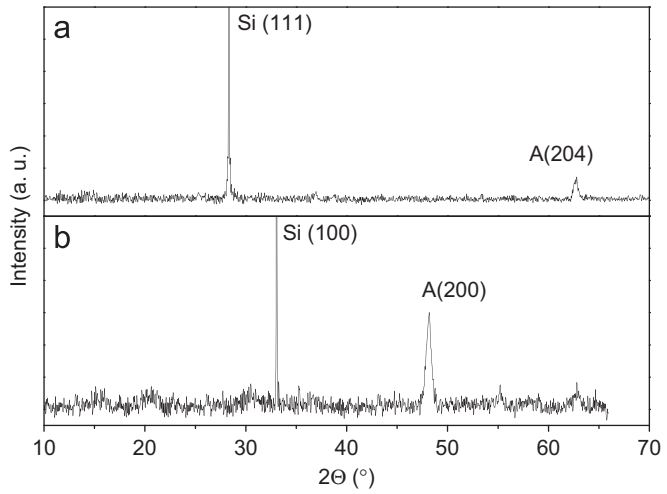

Fig. 13. XRD patterns of $Ti_{1.825-x}Nb_xO_4$, $x=0.03$ thin films fabricated on (a) Si (111) and (b) Si (1 0 0) substrates from nanosheets followed by heating at 700 °C in air for 5 h.

formation of rutile, see insert to Fig. 11b. The changes in morphology during the conversion process were examined by tapping-mode AFM of re-dispersed and deposited materials, Fig. 12a–c. Surprisingly, two-dimensional nanosheets with thickness of 1 nm are still found for the sample annealed at 500 °C for 2 h. Upon extended annealing, the number of sheets is reduced while the number of small crystallites increases. After calcination at 900 °C (Fig. 12c), no 2D-like morphology is any longer observed and the dispersed particles take a more rod-like nature. The fact that the weight loss is complete at 500 °C as seen by TGA (inset Fig. 10), suggests that the sheet-like material is either a lepidocroicite related oxide or an anatase-like material (Fig. 9a) as indicated by the diffraction data.

3.4. Thin films fabricated from nanosheets

Nb-substituted titania thin films were prepared by spraying of nanosheets (TBA-$Ti_{1.825-x}Nb_xO_4$, $x=0.03$) onto hot Si(100) and Si(1 1 1) substrates followed by heat treatments at 700 °C in air for 5 h. The XRD patterns, Fig. 13, show preferential growth of the obtained anatase as evidenced by the observation of anatase (2 0 0) for Si(1 0 0) and anatase (2 0 4) for Si(1 1 1). The thickness of the films is estimated by depth analysis (Nanoscope V612) from AFM images. The average thickness obtained by spraying for 1 min is 40–50 nm, increasing to 100 nm by prolonged spraying for 4 min. AFM tapping mode images, Fig. 12d-e, show a surface topography consisting of interwoven 2D-octahedra having quite identical size and smooth surfaces with the average roughness of 3.8 nm.

4. Conclusion

Single-layered Nb-substituted titanate nanosheets with a thickness of ca. 1 nm were successfully obtained by exfoliating TBA-intercalated Nb-substituted titanates in water. AFM images and turbidity measurement reveal that the exfoliated nanosheets crack and corrugate when exposed to a long time sonication. The Nb-substitution suppresses the transition from nanosheets into anatase and notably also from anatase to rutile. The transformation temperature of the maximum Nb-substituted anatase materials to rutile is around 900 °C, much higher than earlier found for Nb-doped nanoparticles. The latter aspect may appear essential for technological application of thin anatase coatings. Highly oriented Nb-substituted sprayed materials were obtained from the layered precursors via delamination, reconstruction and subsequent heat treatment. Dependent on the atmosphere during calcination, the incorporation of Nb into TiO_2 induces different defects and hence also electronic situations. This provides additional degrees of freedom to tailor physical properties of $(Ti,Nb)O_2$ powders and coatings. At reducing conditions, Nb is incorporated as Nb^V and an equivalent amount of Ti^{IV} is transformed to Ti^{III}. By heating in air the Ti^{III} ions are oxidized to Ti^{IV} and the incorporated Nb^V is anticipated to be charge compensated through cation vacancies.

Acknowledgments

The authors acknowledge financial support from the Research Council of Norway (NANOMAT, Grant no.163565 431). Valuable assistance with AFM and SEM measurements by Oddvar Dyrlie and Sissel Jørgensen, and with XPS by Martin F. Sunding, all at the Centre for Materials Research and Nanotechnology, University of Oslo, is highly acknowledged. Dr. Pascal Dietzel is thanked for assisting in data collection at ID31, ESRF. Access to beam time is gratefully acknowledged.

References

[1] Z.Q. Song, H.Y. Xu, K.W. Li, H. Wang, H. Yan, J. Mol. Catal. A: Chem. 239 (2005) 87.
[2] Y. Umemura, E. Shinohara, A. Koura, T. Nishioka, T. Sasaki, Langmuir 22 (2006) 3870.
[3] S. Nakano, T. Sasaki, K. Takemura, M. Watanabe, Chem. Mater. 10 (1998) 2044.
[4] T. Sasaki, M.J. Watanabe, Am. Chem. Soc 120 (1998) 4682.
[5] A.F. Reid, W.G. Mumme, A.D. Wadsley, Acta Cryst. B24 (1968) 1228.
[6] D. Groult, C. Mercy, B. Raveau, J. Solid State Chem. 32 (1980) 289.
[7] A. Verbaère, M. Dion, M. Tournoux, Rev. Chim. Minér. 12 (1975) 156.
[8] M. Hervieu, B. Raveau, Rev. Chim. Minér 18 (1981) 642.
[9] T. Birchall, N.N. Greenwood, A.F. Reid, J. Chem. Soc. A 16 (1969) 2382.
[10] T. Gao, H. Fjellvåg, P. Norby, J. Mater. Chem. 19 (2009) 787.
[11] H.Y. Song, A.O. Sjåstad, Ø.B. Vistad, T. Gao, P. Norby, Inorg. Chem. 48 (2009) 6952.
[12] Y. Furubayashi, T. Hitosugi, Y. Yamamoto, K. Inaba, G. Kinoda, Y. Hirose, T. Shimada, T. Hasegawa, Appl. Phys. Lett. 86 (2005) 252101.
[13] Y. Furubayashi, T. Hitosugi, T. Hasegawa, Appl. Phys. Lett. 88 (2006) 226103.
[14] O. Carp, C.L. Huisman, A. Reller, Prog. Solid State Chem. 32 (2004) 33.
[15] M. Valigi, D. Cordischi, G. Minelli, P. Natale, P. Porta, J. Solid State Chem. 77 (1988) 255.
[16] K.J. Sakata, Phys. Soc. Japan 26 (1969) 1067.
[17] H. Yamada, R.G. Teller, I. Song, Mater. Res. Soc. Symp. Proc 138 (1989) 185.
[18] Q.L. Wu, A.O. Sjåstad, Ø.B. Vistad, J. Roots, P. Norby, J. Mater. Chem. 15 (2005) 4695.
[19] N. Sukpirom, M.M. Lerner, Mater. Sci. Eng. A 333 (2002) 218.
[20] T. Sasaki, M. Watanabe, H. Hashizume, H. Yamada, H. Nakazawa, J. Am. Chem. Soc. 118 (1996) 8329.
[21] K. Fukuda, Y. Ebina, T. Shibata, T. Aizawa, I. Nakai, T. Sasaki, J. Am. Chem. Soc. 129 (2007) 202.
[22] J. Arbiol, J. Cerdà, G. Dezanneau, A. Cirera, F. Peiró, A. Cornet, J.R. Morante, J. Appl. Phys. 92 (2002) 853.
[23] A.M. Ruiz, G. Dezanneau, J. Arbiol, A. Cornet, J.R. Morante, Chem. Mater. 16 (2004) 862.